Chapter 1

Introduction

In 1967, the first detection and identification of stable pulsations from celestial sources by Jocelyn Bell opened up one of most fascinating areas in radio astronomy (Hewish et *al.*, 1968). Significant advances have been made to date in understanding these objects, the pulsars. In this chapter, we outline our present understanding of the radio emission from pulsars, more specifically their average and single-pulse properties. We review different phenomena occurring at single-pulse time-scales and available conventional tools to study them. Most of these studies have been carried out so far at meter and decimeter wavelengths. Observations at low radio frequencies pose severe challenges; and we discuss these considerations in the third section. In the last section, we discuss the sensitivity aspects of a radio signal and its detection.

1.1 Pulsars as astronomical objects

Over a thousand radio pulsars have been discovered in our Galaxy so far and their nature as compact, rotating, highly magnetized neutron stars is well established. The radiation is beamed along the magnetic axis, where the rotational and magnetic axes are not aligned. This results in a lighthouse effect; as (and if) this cone sweeps across an observer, a radio pulse will be observed. The estimated properties of neutron stars from various measurements are: mass $\sim 1.4 M_{\odot}$, radius ~ 10 km, surface magnetic field $\sim 10^{12}$ G, etc.

1.1.1 Basic model

Figure 1.1 shows the basic model of the pulsar phenomenon. The neutron star possesses a strong magnetic field which is dipolar, where the field lines are rigidly anchored to the star and the associated magnetosphere tries to corotate with the star. Corotation with the star is not possible

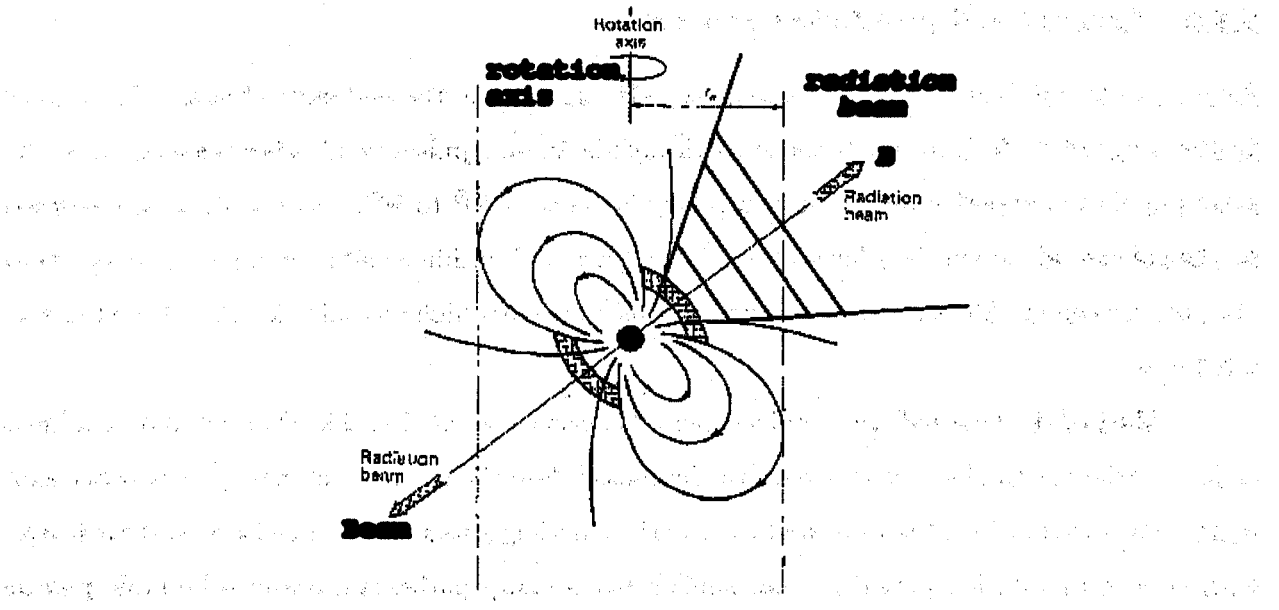

Figure 1.1: Basic model of a pulsar as a rotating, magnetized neutron star.

beyond a certain distance, r_{LC}, where the rotation speed equals the speed of light. The field lines that manage to close inside form the 'closed magnetosphere', while the rest of the field lines extend into the interstellar regions, and are referred to as 'open field lines'. The emission cone is believed to be defined by the tangents at the location of emission to the last open field lines that do not close. It is believed that primary charge particles are generated and accelerated very close to the stellar surface. These accelerated particles in the presence of magnetic field lead to a cascade of pair production reeulting in a relativistic and dense plasma in the polar region. This 'secondary' plasma, moving relativistically along the open dipolar field lines, gives rise to the observed radio emission. This charge particle flow and the (low frequency) dipole radiation carries away the rotational energy, effecting a 'braking torque' on the star. Both the above mechanisms are likely to be present, resulting in the secular loss of rotational energy of the pulsar. Such an energy loss E scales as $\propto B_0^2 R^6 \Omega^4$, and pulsar periods lengthen with their age.

The radio emission is a very small fraction ($\lesssim 10^{-6}$) of the total rotational energy loss, and the exact mechanism of emission is still a debated issue. The implied brightness temperatures for the pulsed radio emission require the emission to be coherent. The primary physical constraints on a model are provided by the total observed flux and its spectrum, small duty-cycles ($\sim 4\%$), and observed polarization and fluctuation phenomena.

1.1.2 General and population properties

Neutron stars are believed to originate in type-II supernovae, the end state of stars with masses in the range of 8–15 $M_{\odot}$. From the statistics of the known pulsars and other neutron stars, the total population of active pulsars in our galaxy is between 10^5 to 10^6. Most of them are confined to the galactic plane within a layer about 1 kpc thick and within a radial distance of 10 kpc from the galactic center. Measurements show that pulsars possess high spatial velocities of the order of 200 km/s.

Most of the "normal" pulsars have periods between to 0.1–2 s. The shortest known value is $\sim$ 16 ms, whereas the longest is $\sim$ 8 s. All the pulsars lose their rotational energy, and hence slow down. The distribution of periods and their derivatives suggests that most pulsars start their lives with very short rotation periods, follow similar evolutionary paths, and cease to be radio pulsars after $\sim 10^7$ years. Equating the loss in rotational energy with the dipole formula ($I\Omega\dot{\Omega} \equiv B_0^2 R^6 \Omega^4$) yields $\dot{\Omega} \propto \Omega^3$, and also provides a way to estimate the magnetic field of a pulsar.

The normal measure of the slow-down of pulsars is $\dot{P}$, a dimensionless quantity typically of the order of 10^{-15}, often quoted in units of s/s. The phenomenological slowing-down relationship

$$\dot{\Omega} = -K\,\Omega^n \tag{1.1}$$

defines the "braking index" n (= 3 for spin-down due to magnetic dipole radiation), and integrating it gives us

$$T = -(n-1)^{-1}\left(1 - x^{n-1}\right)(\Omega/\dot{\Omega}), \tag{1.2}$$

where the coupling constant K was removed by using the eq. 1.1. The quantity $x \equiv \Omega/\Omega_0$, where Ω_0 is the spin rate at birth. If x is small and n=3, we obtain the estimate for the "characteristic age" of the pulsar, $T = P/2\dot{P}$.

On a time-scale of some days, all pulsars show a remarkable stability in rotation rate. There is, of course, the slow-down torque of the magnetic dipole radiation , or an associated particle wind, causing a steady increase in period. Careful measurements of pulse-arrival times over long intervals show that a pulsar period is more stable than 1 part in 10^{12}. These measurements have to be corrected for a number of effects, such as the motion of Earth around the Sun, dispersion delay at the observing frequency, and relativistic clock correction, etc. If the period of a pulsar is known to a sufficient accuracy, one can predict the pulse arrival time in the future. Such studies of pulsar rotational parameters are termed as 'pulsar timing', which allow very accurate measurements of pulsar period, period derivative, and its location in the sky.

There is a separate population of pulsars, called 'millisecond pulsars' (MSPs), with periods mostly below 10ms. MSPs belong to an older population of the neutron stars, and have weaker magnetic fields. They are less confined in the galactic plane, and believed to possess a different life history, discussed more in chapter 6. Many are found in binaries and in globular clusters and are visible as radio pulsars over a longer life-span (relative to normal pulsars) due to their very weak magnetic fields.

1.1.3 Average pulse properties

The integrated-pulse profiles are obtained by superimposing a sequence of typically 1000 individual pulses. The average properties provide information about the stable properties of the pulsar radio emission, such as the flux densities, radio frequency spectra, emission-beam structure and viewing geometry etc.

Integrated profiles

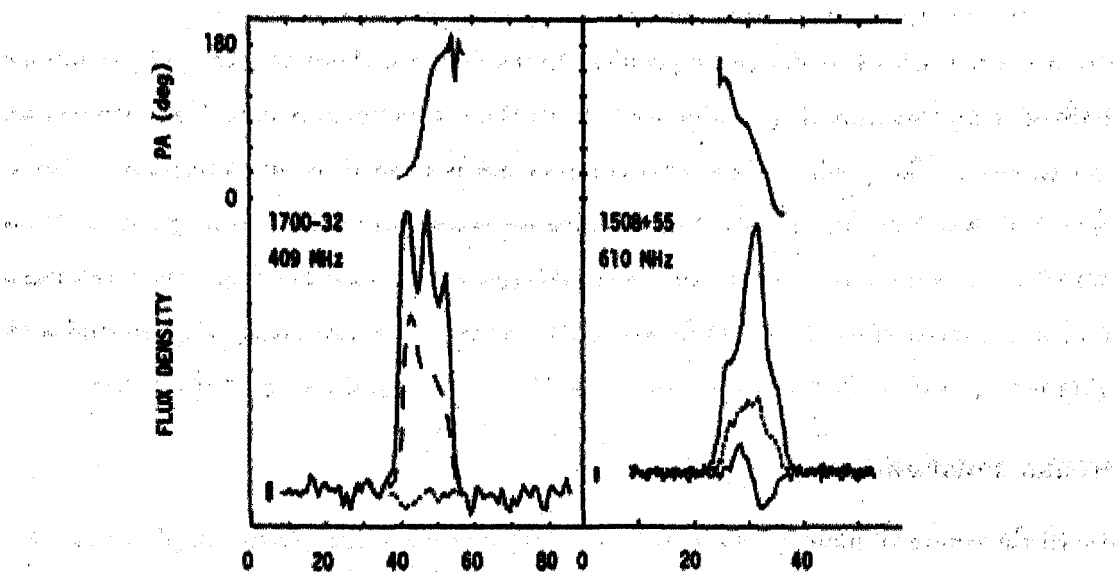

Figure 1.2: Mean-pulse profiles and polarization parameters for two pulsars. The 'S'-curve traced by the position angle of the average polarization is evident. Average polarization is more than 50% at certain locations in the pulse. The circular polarization in B1508+55 shows a change in its sign close to the midpoint of the profile. (Lyne & Manchester, 1988)

Integrated-pulse profiles and polarization parameters of two pulsars B1700–32 and B1508+55 are shown in figure 1.2. The intensity profiles are generally smooth curves, generally up to three components, more rarely with four or five. By cgnvention, one pulsar period (P_1) is equal to 360° of rotational longitude, usually denoted by φ. . The pulse widths lie between 5-30" in rotational

longitudes.

Separate components of emission often appear as discrete sources of emission. Pulsar emission is highly linearly polarized. The individual pulses tend to display a high degree of polarization, which may sometimes get averaged over to a smaller degree in the integrated pulse profiles. However, the integrated pulse polarization approaches up to 100% in some pulsars. As shown in figure 1.2, the position angle of the linear polarization swings in a characteristic S shape, covering most of the 180° range. Even in the profiles with multiple components this polarization swing is continuous through the entire profile, and this behavior does not change with the frequency of observation. This, following Radhakrishnan & Cooke (1969), is taken as a suggestion that the observed polarization is related to the dipolar structure of the magnetic field, and that the radiation is generated close to the magnetic poles. This radiation is emitted in a narrow, hollow cone radially outward and is centered on the magnetic axis. Different components of the average profile then arise from the structure in this polar emission region and the observer's viewing geometry.

Although the pulses from the majority of pulsars occupy only about 10° of rotation phase, there are a few with broader pulse profiles. In some cases, there are two pulse components which are distinct and separated by about 180°. Both the components behave like a single pulse of most other pulsars. The weaker of the two components is termed as an 'interpulse'. The clear cases of interpulses are usually interpreted as emission beams from the two magnetic poles of a pulsar whose rotation and magnetic axes are near-orthogonal to each other (*e.g.* the Crab pulsar). There are also instances of interpulse emission when the two axes are nearly aligned and a single polar region is responsible for both, the "main" and the "inter"-pulse (*e.g.* B0950+08).

Circular polarization

Toward the center of many profiles, and especially those resulting from sampling close to the center of the emitting cone, there is often a high degree of circular polarization. The degree of circular polarization often reaches 10% at the center. Frequently it reverses its sign at the center of the profile ; usually there is only one such reversal under the pulse.

Radio frequency dependence

Pulsars are weak radio sources, with average flux-densities at meter wavelengths $\lesssim 1$ Jy. Overall, the flux density spectra are steep at high radio frequencies, though they often flatten or even turn over at $\sim$ 100 MHz. The spectral indices, (a) lie in the range of 1 to 4 ($S \propto \nu^{-\alpha}$), and for some bright pulsars these power laws have been traced all the way up to 35 GHz (Wielebinski et *al.*, 1993).

The shape and the width of all integrated profiles vary considerably over the radio spectrum (see figure 1.3). Apart from the differences in the profile arising from the different spectral indices of various components, there is a general 'expansion' of the whole pulse at lower frequencies ($\lesssim$ 1 GHz). This 'expansion' can often be fitted by a power law, in which the separation between identifiable components, or the pulse width as measured between the outer half-power points of the profile, vary as $\nu^{-\alpha}$. The value of a varies between 0.2 and 0.5 for frequencies below 1 GHz, with an average value of 0.25. The index tends to zero above 1 GHz.

Despite all the changes, the underlying swing of position angle in the linear polarization follows the same pattern at all frequencies, and provides us with information about the geometry of the emission region.

Radius-to-frequency mapping & emission altitudes

As seen above, the epacing of the average-pulse profile components and pulse width as measured between the outermost half-power points of the profile, vary with frequency typically as $\sim \nu^{-0.25}$. One interpretation of such an evolution is (after Komesaroff, 1970, and Cordes, 1978) that different frequencies are emitted at different heights from the stellar surface. The higher radio-frequency radiation is emitted close to the star and the progressively lower frequency emission comes from farther away along the magnetic (open) field lines. Most agree that the emission region is confined within $\sim$ 1000 km from the star, whereas the source of high frequency radiation ($\sim$ 1 GHz) is located close to the polar surface ($\gtrsim$ 10km, according to Rankin, 1990). The emission cone is defined by the directions of 'local' tangents to the magnetic field lines. The dipolar flaring of the magnetic field lines results in a larger angular radius (p) of the emission cone at farther distances from the star's surface whereas, the impact angle (the closest approach' to the magnetic axis) of the observer's line-of-sight (β) remains the same. This changing β/ρ ratio explains the observed pulse width evolution at lower frequencies, as shown schematically in figure 1.5.

If, for example, the radiation at some height were to occur at the local plasma frequency, then the r^{-3} dependence of the plasma density for a dipolar field implies that $\nu \propto r^{-3/2}$. The dipolar field lines flare so that $\mathbf{A0} \propto r^{1/2}$. If the same field lines define the emission cone at all frequencies — *i.e.* at all heights —, then $\mathbf{A0} \propto \nu^{-1/3}$. The flattening of the curve $\Delta\theta(\nu)$ at high radio frequencies would imply a breakdown of the RFM close to the star, or that some other angular scale like the size of the cone for radiation from single particles becomes important.

In this picture, the low frequency emissiqn from .a pulsar originates further away from the surface. Due to a lower β/ρ-ratio, the line-of-sight at low frequencies samples the emission cone more

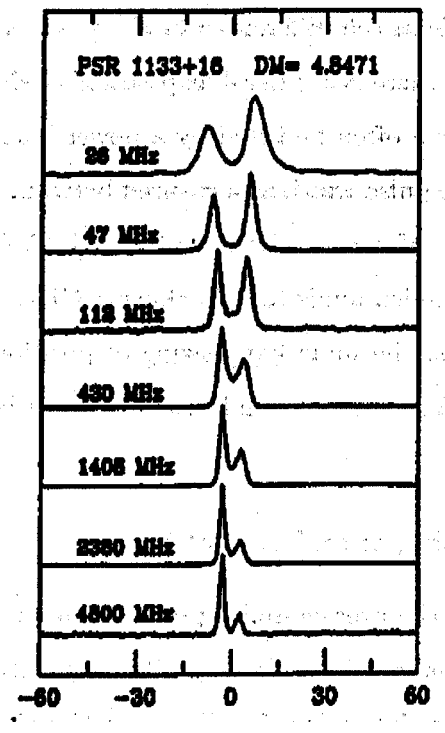

Figure 1.3: Time-aligned multi-frequency profiles of PSR1133+16 (Phillips & Wolszczan, 1992). Notice the evolution of the half-power pulse-width, as well the component separation, with the frequency of observation noted on the left of each profile.

centrally and is therefore expected to provide independent information about the radio-emission region.

Pulsar viewing geometry

Most widely accepted emission models assume that pulsar radiation is emitted over a (hollow) cone centered around the magnetic axis. Figure 1.6 is a schematic illustration of pulsar emission cone. The cone, with a half-opening angle ρ_ν, sweeps across the observer's line-of-sight with an impact angle (distance of closest approach to the magnetic axis) β. The rotational and magnetic axes are inclined with an angle a. The spherical triangle **PQS** (refer to figure 1.6) relates the angles α, β and the profile half-width $\Delta\psi_\nu$ to the beam radius ρ_ν by the following relation (Gil, Gronkowski, & Rudnicki 1984),

$$sin^2(\rho_\nu/2) = sin^2(\Delta\psi_\nu/2)\, sin(\alpha)\, sin(\alpha+\beta) + sin^2(\beta/2) \qquad (1.3)$$

The sweep of linear polariaation across the profile Conforms more or less to a simple pattern dictated by the configuration of the rotation axis, the magnetic axis, and the observer's line-of-sight.

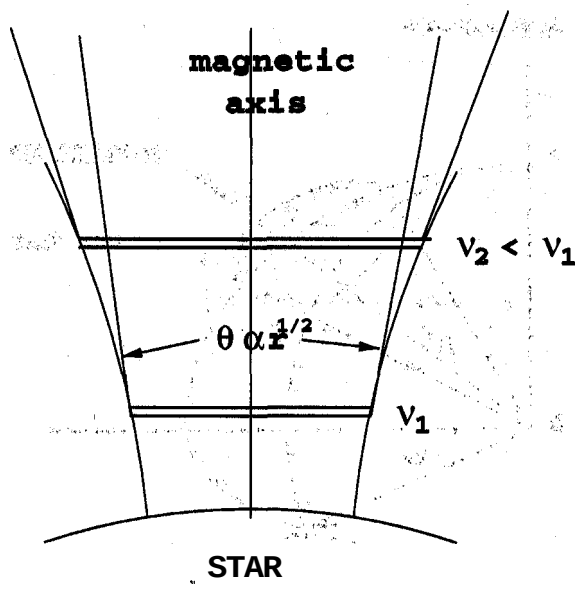

Figure 1.4: A schematic of RFM: different frequencies arising at different heights from the star can cause the frequency dependence shown in figure 1.3.

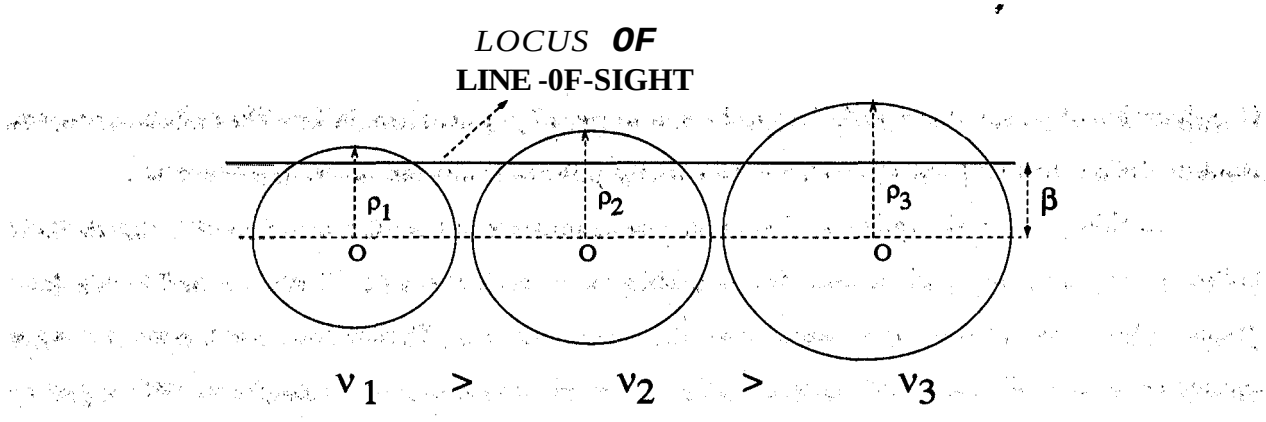

Figure 1.5: A schematic of changing β/ρ as a result of RFM. Due to the increase in the beam radius, the locus of the line-of-sight cuts the beam more centrally relative to the periphery.

In figure 1.6 the polarization position angle χ is given by

$$\tan(\chi - \chi_0) = \frac{\sin(\alpha)\sin(\varphi)}{\sin(\alpha+\beta)\cos(\alpha) - \cos(\alpha+\beta)\sin(\alpha)\cos(\varphi)} \quad (1.4)$$

where χ_0 is the poaition angle of the projected direction (on the sky plane) of the pulsar rotation axis, φ is the longitude, defined such that it is equal to zero on the magnetic meridian.

The maximum of the sweep rate of the polarization angle χ occurs close to the mid-point of the profile (i.e. at $\varphi = 0°$, and is given by,

$$|d\chi/d\varphi|_{max} = \sin(\alpha)/\sin(\beta) \quad (1.5)$$

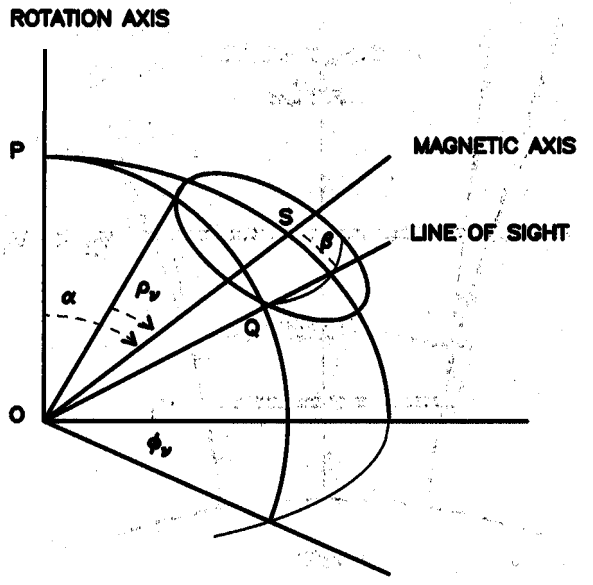

Figure 1.6: Pulsar viewing geometry: the line-of-qight cuts the emission cone of radius ρ_ν with an impact angle of β.

1.1.4 Empirical theory of pulsar radio emission

Classification of pulsar characteristics has been a source of physical insight into the emission process. Rankin, 1983a, has laid out of a scheme to classify pulsars from their average properties.

In this scheme, the pulsar emission pattern comprises of'two distinct elements: one or more hollow cones, and an axial or core beam within these hollow cones. The core and cones have distinct observational properties associated with them (Lyne & Manchester, 1988, however argue against such an explicit distinction and consider the various components as simply a result of patchy illumination). Figure 1.7 represents the geometry of core and cones.

The core components:

- These often have a steeper spectrum than the conal components and dominate at frequencies around 400 MHz and below.
- They exhibit circular polarization and the handedness often reverses sign near the center of the pulse.
- Many have featureless ("white") fluctuation spectra, though in some eases broad, low frequency modulation features are observed in their spectra.
- They are not known to be associated with nulling or mode-changing phenomenon.

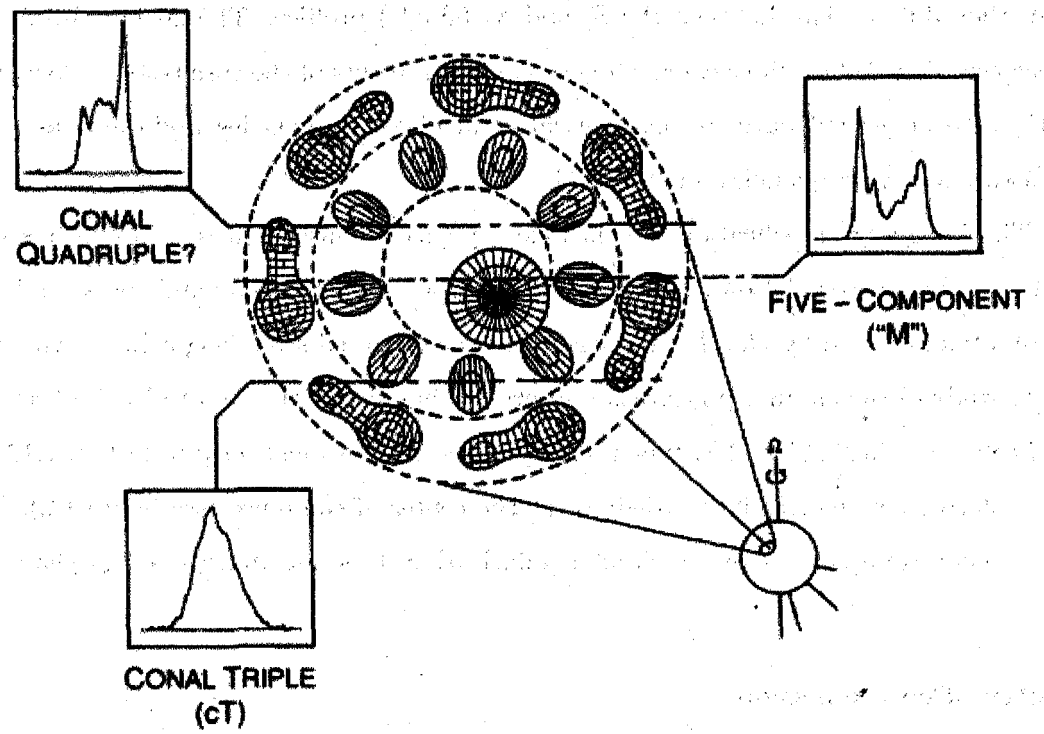

Figure 1.7: Rankin's empirical scheme of central core and conal beams: The variety in the shapes of the integrated profiles of pulsars can be traced to different intersections of the conal beam with the locus of the observer's line-of-sight.

The conal components:

- They show strong linear polarization with the characteristic 'S'-shaped swing of the polarization angle.
- They depolarize at the edge of the profile.
- They show drifting subpulses and other types of periodic modulations.

The core radiation need not be axial; it can be found in a given case anywhere within the cone, superimposed on it, or perhaps, in rare cases, even just outside it. More than one conal beam is required ta explain the complex average profiles containing 5 or more components. The relative intensities of the core and conal components, from various conal rings, vary markedly with frequency as well as from object to object.

Five major categories of pulsar profiles were identified, the core-single (S_t), conal single (S_d), double (D), triple (T), and five-component (M). In such a scheme, the number of components observed in an average profile depends on the viewing geometry of the observer, given by β and ρ.

One can then differentiate between the S_t and S_d (single) profiles. The latter arise from shallow cuts near the edge of the hollow cone, while the former are cuts of the core beam at low frequencies. Thus, the core singles will develop conal 'outriders' at higher frequencies, and the conal components will bifurcate at low frequencies due to RFM.

The foregoing classification also has clear physical consequences. Rankin has noted that there is a significant correlation between the different classes of pulsars and the so-called 'acceleration potential', defined by B_{12}/P^2, the ages, and the observed scale height in the Galaxy.

A study of the circular polarization in profiles has shown that most of it is observed in core components — *i.e.* in S_t, T, and M-type pulsar profiles. As was mentioned in section 1.1.3, typically circular polarization changes its handedness at the center of the pulse (see figure 1.2). There are, however, many examples where the circular polarization does not undergo a sign change within a pulse.

Geometry of core emission

Rankin (1990) studied a group of interpulsars for their core emission. These pulsars were chosen since it is for these pulsars that the angle α is known reliably to be close to 90°. For six pulsars from the sample analysed, the core component widths (W_{core}) could be measured with reasonable accuracy and those were interpolated to 1 GHz. When plotted against period, these values exhibit a surprisingly accurate power-law relation. A least-squares fit to these values yielded the result that $W_{core} = 2.45°/\sqrt{P}$. The core components of ,most other interpulsars also have widths comparable to those given by the above relation. Figure 1.8 shows the observed pulse-width plotted against the periods of pulsars containing a core components.

This core width-period relationship has been argued to have a very simple interpretation in terms of the magnetic field structure of the pulsar. Assuming a dipolar magnetic field, the angle p between the magnetic field-line tangent and the magnetic axis can easily be evaluated. Taking the 1-GHz width of the core component as twice the ρ-value, it was shown that

$$W_{core} = 2\rho \approx 2.49°\sqrt{r/R}/\sqrt{P},$$

where r is the emission height measured from the center of the star, and R is the stellar radius, assumed to be 10 km.

Comparing the empirical relationship for W_c with the geometrically derived expression for W_{core} above, both equations have a $P^{-1/2}$ term, and thus it appears that the period dependence of the core-width is geometrical in origin. However, the two expressions can be reconciled numerically only if $r \sim R$. This is taken to imply that the core-component emission comes from regions close

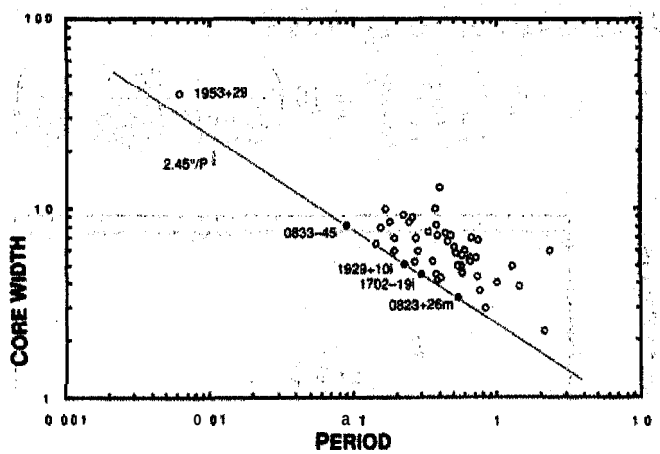

Figure 1.8: Half-power width of 50 core-single pulsars plotted as a function of period. The symbols of a few prominent pulsars are labeled, and those with interpulses are indicated by a filled symbol. The indicated curve is $2.45°/\sqrt{P}$, (see text) (from Rankin, 1990).

to stellar surface.

Most pulsars do not have interpulses. Simple arguments (see Rankin, 1990) suggest that the above relation of core-widths can be generalized to any pulsar with a core component

$$W_{core}(1\,GHz) = 2.45° P^{-1/2}/sin(\alpha) \tag{1.6}$$

Thus, a simple relation relates the observed core-widths to a. The core component originates close to the star, at a height of ~10 km, and for a general case the above relation can then be inverted to obtain the value of a.

The plot of core-width against the period for triple interpulsars shows that their core-widths obey the relation, within the measurement errors, very closely. For all other pulsars of S_t-, M- and T-type, widths of the core components fall above the curve that indicates the fitted widths of the interpulsars.

Geometry of canal emission

As we just discussed, in the case of pulsars with core components, the value of a could be estimated. To study the geometry of conal emission we refer to the geometry described in section 1.1.3. From eq. 1.3 we can derive the following,

$$\rho = cos^{-1}[cos(\beta) - 2\,sin(\beta)\,sin(\alpha+\beta)\,sin^2(\Delta\psi/2)] \tag{1.7}$$

On the premise that the core emission is produced close to the star ($r = R = 10$ km), the emission height of the conal emission at 1 GHz can be estimated assuming a dipolar field geometry

in the entire emission region via the following relation,

$$h_{1GHz} = 10.\left(\frac{2\rho}{W_{core}}\right)^2 = 10\left(\frac{2\rho}{2.45°P^{-1/2}/sin(\alpha)}\right)^2 \quad (1.8)$$

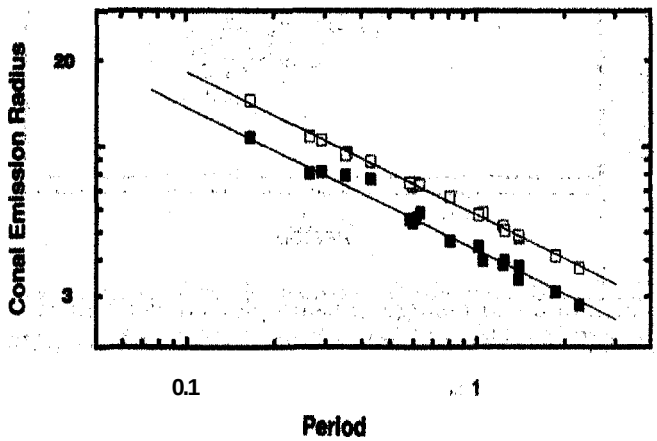

Figure 1.9: Conal radius ρ plotted as a function of period for the 'inner' (solid symbols) and 'outer' (open symbols) conal zones of five-component (M) pulsars. The curves of $4.3°/\sqrt{P}$ and $5.8°/\sqrt{P}$ are indicated (from Rankin, 1993).

Using the above relationships, conal geometry for the M-type pulsars (five-components) could be calculated with some confidence, owing to the presence of both a core component and two conal rings. The 1-GHz angular radii of the two conal zones was found to exhibit a very regular behavior. They also scale as $P^{-1/2}$ as follows:

$$\rho_{inner} = 4.3°P^{-1/2} \quad (1.9)$$

$$\rho_{outer} = 5.9°P^{-1/2} \quad (1.10)$$

Figure 1.9 shows the' pulse-widths plotted against the periods in the case of the M-type pulsars. The fitted curves are indicated. The agreement between all the pulsars is remarkable, and eq. 1.6 remains an enigmatic relation yet to be explained by any physical models.

Because both the core and conal widths scale as $P^{-1/2}$, the emission height is seen to be independent of the period. The above relationships then translate into emission heights of:

$$h_{inner} = \sim 120\ km \quad (1.11)$$

$$h_{outer} = \sim 210\ km, \quad (1.12)$$

where, it is assumed that the inner and outer conal emission occurs along the same set of magnetic field lines (*i.e.* the last open field lines), which is not necessarily true.

These results for M-type pulsars were compared with the other pulsars of T- and S_t-type, which have a core component surrounded by a conal ring of emission. Exactly same procedures were employed to obtain estimates of conal radius ρ. Such a plot (like figure 1.9) shows an overall $P^{-1/2}$ trend with significant departures. S_t-stars usually lie closer to the lower curve, whereas the T-type stars show less orderly behavior. Results for the S_d, D, and cT pulsars show that these objects also obey the general $P^{-1/2}$ trend very closely.

Core emission then occurs in a majority (60-'70%) of mostly younger population of pulsars, whereas the conal emission dominates in the remaining older population. The above work (Rankin 1990) showed that the core-widths are related to period, and emission geometry, which could be inverted to get the angle a. The magnitude of the widths allow us to estimate the heights of the emission. Rankin (1990) concluded that the core emission occurs close to the stellar surface, whereas the conal components for 1 GHz occur at height of $\sim 100 - 200$ km. The lower frequency conal emission would come from progressively larger heights in the magnetosphere. Rankin associated the conal emission to relatively high-γ particles ($\gtrsim 200$) and core emission to particles with $\gamma \sim 20$.

Pulsar beams: circular, nested cones

Several attempts were made to model the pulsar beam shapes using the data on an ensemble of pulsars. Based on their study; Narayan & Vivekanand (1983) concluded that the beam is elongated in the latitude. Lyne & Manchester (1988), on the other hand, have argued that the beams are essentially circular, Based on the dipole geometry of the cone of open field lines, Biggs (1990) found that the beam shape is a function of the angle (a) between the rotation and the magnetic axes. Mitra & Deshpande (1999) modeled the shape of pulsar emission beams within the framework drawn above by using a carefully selected subset of the multi-frequency polarimetric observations of 300 pulsars (Gould & Lyne, 1998). They assumed an elliptical beam shape in general, and that the beam size depends on a. They chose pulsars with 'T' and 'M' profiles, which contain a core component, which allowed them to estimate the viewing geometry. A self-consistent model was sought after solving for the dependence of ρ on the observing frequency ν.

They did not find any evidence for any beam compression, and data were consistent with circular beams for all values of a. They identified three nested cones of emission in the form of nested rings whose widths are typically 20% of the respective cone radii.

1.2 Single-Pulse properties

The stability of the average properties, discussed above, manifests the stationary structural property of the emission region within the polar flux tubes above the magnetic polar cap. Each single pulse, however, is vastly different from the average profile.and other pulses, in general. Individual pulses show discrete entities of emission in the pulse region, termed 'subpulses'. The widths of subpulses typically lie between 1°-5° of longitude (see,figure 1.10 for an example of single pulses from pulsar B0834+06). In fact, the statistical distribution (locationand frequency of occurrence) of subpulses determines the integrated pulse profiles. The subpulses are regarded as basic components of emission from discrete sources, and their longitude location in the pulse can be interpreted as a physical distribution at the polar emission region.

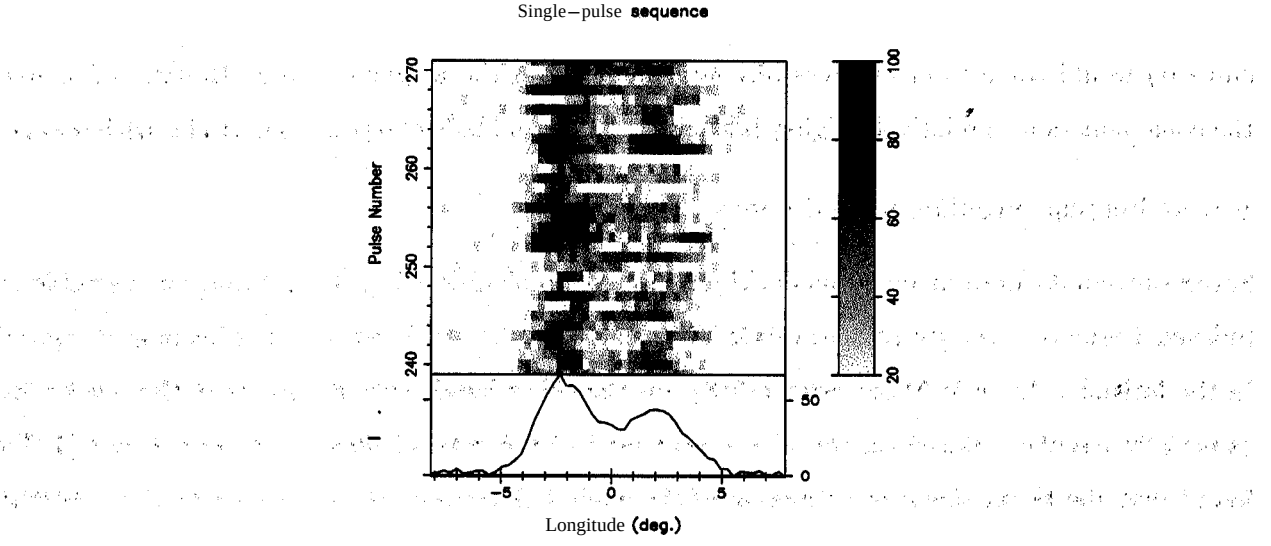

Figure 1.10: Single pulses from B0834+06 at 327 MHz. Notice that the emission in each individual 'pulse is chiefly confined to narrow subpulses.

There is also structure on much shorter time scales, typically $\sim 1\mu$ s, called as 'microstructure'. Groups of well-separated narrow features, sometimes periodically spaced in a pulse window, may occur in a single pulse.

Subpulses, and even micropulses, show a high degree of polarization. The linear polarization position angle sweeps across in a subpulse by typically less than $\sim 30°$, and these combined with shifts in the location of individual subpulses often result in a depolarization of the integrated profile.

As a general case, subpulses fluctuate in their amplitude and their location in the average pulse window. It is just such phenomena related to the subpulse fluctuations and modulations that we will discuss in detail now.

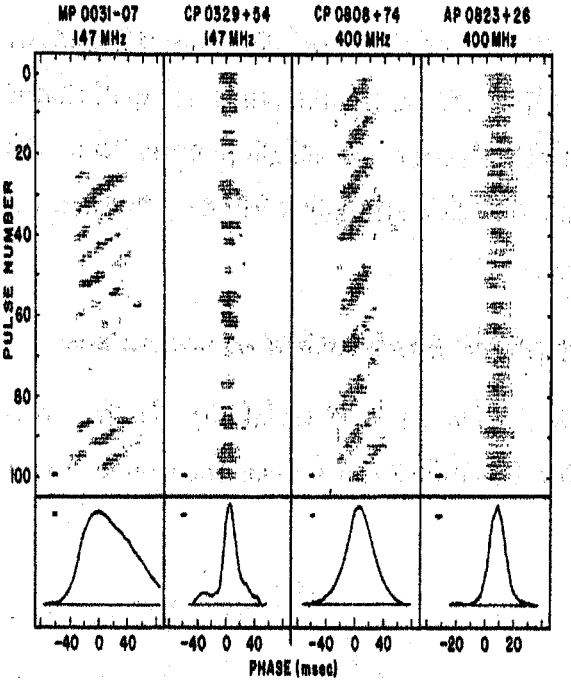

Figure 1.11: Individual pulses displaying subpulse drift and nulling (from Taylor & Huguenin, 1971). Notice for B0031-07, the first 20 pulses are in a 'null' state, and shorter nulls seem to be present in the sequence of B0329+54.

1.2.1 Individual pulse intensities and nulling

Many pulsars show a distribution of total pulse energies which resembles a normal distribution around the average value (*e.g.* , B1642–03). Others like B0950+08 display an asymmetric distribution peaking at low values and a long tail at high energies. The Crab pulsar is an extreme case of such a distribution, which shows occasional 'Giant Pulses'. B0834+06 (see figure 1.10 for single pulses from this pulsar) shows a bimodal distribution: there is a finite probability of zero power, and a separate distribution of values about a non-zero energy. The 'zeroes' may 'occur in isolated pulses or in groups, and this phenomenon is termed as 'nulling', and occurs abruptly within even one rotation period (see figure 1.11).

The duration of the nulls, and the interval between two successive occurrences of null pulses, vary randomly about characteristic values. For some pulsars, like B0834+06, short nulls of 1–3 pulses occur once every few tens of pulse periods. For others the null state may last for minutes, or even a majority of the time, like the extreme example of B0826-34, whose nulls last for 70% of the time. Short nulls may, however, at times go unrecognized in weaker pulsars.

Earlier the phenomenon of nulling was believed to be associated to older, long period pulsars. Nulling was believed to represent a total lack of radio emission over a short time duration, and a

precursor to the complete cessation of radio emission from that pulsar. Under the phenomenology of core and cone emission outlined above, Rankin (1986) showed, that the pulsars which null belong to older populations of objects than the core-single pulsars. But, within a given class of objects, the nulling fraction does not correlate strongly with age. Pulsars, therefore, do not seem to null simply by virtue of their age.

1.2.2 Amplitude and phase modulation of subpulses

Subpulse intensities display a wide range of variability, leading to the observed variety in individual pulses. The subpulse variability can be classified under two, types: amplitude and phase modulations.

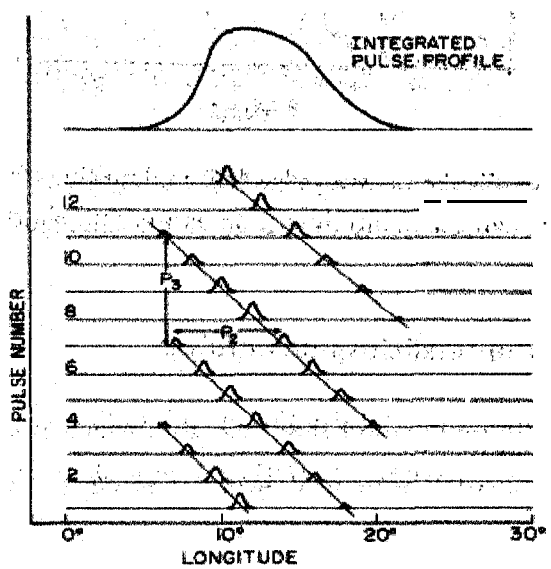

Figure 1.12: A schematic diagram of drifting subpulses: successive pulses appear at the fundamental rotational period of P_1. The pattern of subpulses repeats after an interval P_3. Subpulses are separated by a typical interval P_2 (after Backer, 1973).

In phase modulation, the position of a subpulse within the average-pulse window shifts systematically from one pulse to the next, the phenomenon of 'drifting subpulses', In some pulsars such a modulation results in regular .drift patterns in their individual-pulse sequences, as shown in the case of three pulsars in the figure 1.11. This 'marching' of the subpulses is shown in an idealized schematic in figure 1.12. The pulse period of the pulsar is labeled as P_1, and P_2 is the longitude spacing between consecutive (bands of) subpulses within single pulses. The drift at rate D(= P_2/P_3) brings successive subpulses at the same longitude at intervals P_3. The drift periodicity in time is usually expressed in the units of P_1. The phase modulation is usually associated with

the conal emission, and the drifting pattern is most apparent for S_d profiles, where the sightline is believed to cut the emission cone tangentially.

We refer to Rankin, 1986, for the tabulated values of various parameters in the cases where stable drift patterns are observed. Sgme pulsars show more than one drift rate: in most of these cases the component spacing P_2 does not change, and the change in P_3 is inversely proportional to the drift rate. Two pulsars, B0031-07 and B2319+60, each show three distinct values of drift rate corresponding to three different drift modes.

Periodic modulation is observed in the conal components of D, T and M pulsars without any apparent systematic drift. This behavior can be seen from figure 1.10 in the case of B0834+06. This is easily understood in the following simple picture of conal emission, where stable, discrete entities of emission drift steadily around the magnetic axis. A tangential cut by the locus of our line-of-sight across this cone makes the motion around the magnetic axis appear as subpulse drift. For pulsars like B0834+06, where the cut is almost central to the beam, the emitting regions would seem to move in and out of the observed zone without without any apparent drift in longitude, giving rise to a modulation without a drift, the so-called 'amplitude modulation'.

The modulation depth may change from one longitude to another in the pulse. The ratio of the modulated power to the average power is generally observed to increase at lower frequencies. Observations show that the period of a modulation in a given pulsar does not vary with the frequency of emission.

1.2.3 Subpulse drift and viewing geometry

Figure 1.13 illustrates the geometry of the emission beam of a pulsar envisioned by Ruderman & Sutherland (1975) in order to explain the phase modulation observed in the subpulse pattern. The detailed discussion of the model is deferred to chapter 5.

In this schematic, O is the center of the star and a circular hollow cone of emission is sampled by the line-of-sight of the observer nearly tangentially at points A and B. OQ and OP are the rotation and magnetic axes of the star respectively. The angle between two discrete emission regions is $0 = 2\pi/N$, where N is the total number of such stable, discrete emission entities on the hollow cone.

We can derive the following geometrical relations,

$$AB = 2OR' \sin(\beta) \sin(\theta/2). \quad (1.13)$$

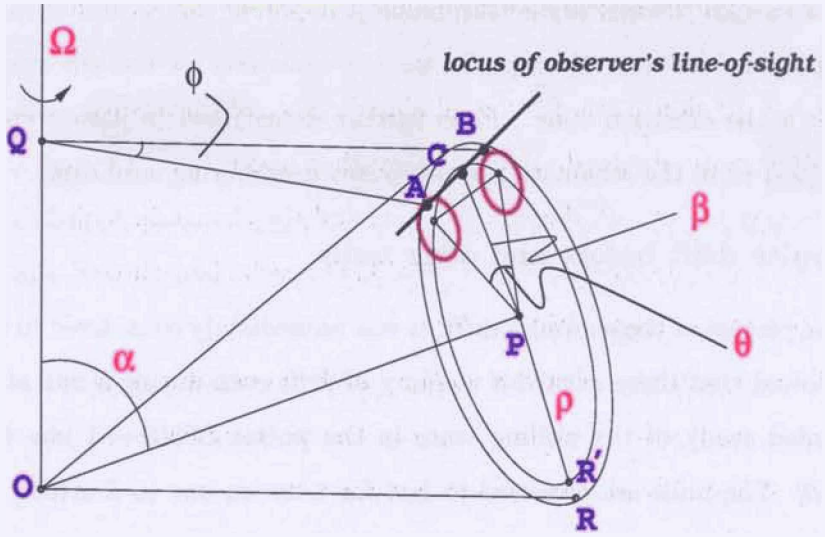

Figure 1.13: Viewing geometry associated with the observed subpulse drift. Discrete entities on the hollow-cone of emission rotate steadily around magnetic axis (defined by OP) of a pulsar. A & B are two such entities, located on the hollow cone of emission (circle ABR) of radius ρ. P is the center of emission region and O the center of the star (our reference frame). OQ is the rotation axis of the star, which is tilted at an angle of α from the magnetic axis OP. ACB is the locus of an observer's line-of-sight, which cuts the emission cone nearly tangentially, at an angle β from the center. ϕ and θ are the angles subtended by ACB in rotational longitude and the magnetic azimuth, respectively.

$$AB \;=\; 2OR' \sin(\alpha+\beta)\sin(\varphi/2) \tag{1.14}$$

Combining the two equations, we can estimate approximately the angular separation θ on the hollow cone for two points with a longitudinal (rotational phase) separation of φ as (see eq. 3 of paper-I),

$$\theta \;=\; 2\sin^{-1}\left[\sin(\alpha+\beta)\sin(\varphi/2)/\mid \sin(\beta)\mid\right] \tag{1.15}$$

Unfortunately, it is usually difficult to determine the values of α and β, and the sign of β is particularly hard to estimate reliably.

Since an observer's sightline samples the emission cone and the emission entities only once in a period, the periodicity of the modulation due to the drift of emission regions around the point P can be aliased. The drift direction is uncertain in this case. A counterclockwise drift around P, from A to B as shown in the figure, is termed as positive drift. A drift in the opposite direction is termed as negative. Two possible values of the drift period are P_3^+ and P_3^- for positive and negative drift, respectively. These two are related by

$$P_3^+ \;=\; \frac{1}{1-\frac{1}{P_3^-}} \tag{1.16}$$

and both the values are always larger than one.

The apparent value of P_2 depends on the centrality of the cut made by an observer's sightline through the emission cone. P_3 is further determined by the circulation time and the angular separation (θ in the schematic) between two neighboring subbeams.

1.2.4 Subpulsa drift before and after nulls

Considering the picture of the subpulse drift, it was immediately considered in the presence of nulls. Cole (1970) showed that there existed a memory of drift even during a null state.

A detailed study of the nulling state in the pulsar B0809+74 was reported by Lyne & Ashworth, 1983. The nulls are observed to last for between one to fourteen pulse periods in the case of this pulsar. In figure 1.14 the phase of the drift would appear as a horizontal line if the drift were unaffected by the null. The plot is a compendium of measurements for a total of 159 nulls of various lengths up to 14 missing pulses. The phase of the drift is clearly related before and after the null; the relation depends, however, on the length of the null.

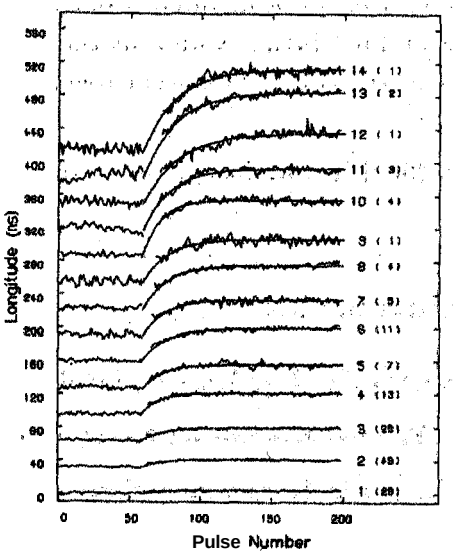

Figure 1.14: The phase of the drifting subpulses at nulls of various lengths in B0809+74. The null length is shown at the right of each track, followed in parenthesis by the number of tracks in each average. The curves are exponential relaxations (Lyne & Ashworth, 1983).

The pattern of drift before and after a null is described by Lyne & Ashworth as follows. There is a small increase in the drift rate just before the null. Immediately after the null starts, the drift stops and then exponentially recovers to its former value. The time constant of this recovery depends on the length of the null; it is about 10 seconds for short nulls and 20 seconds for long

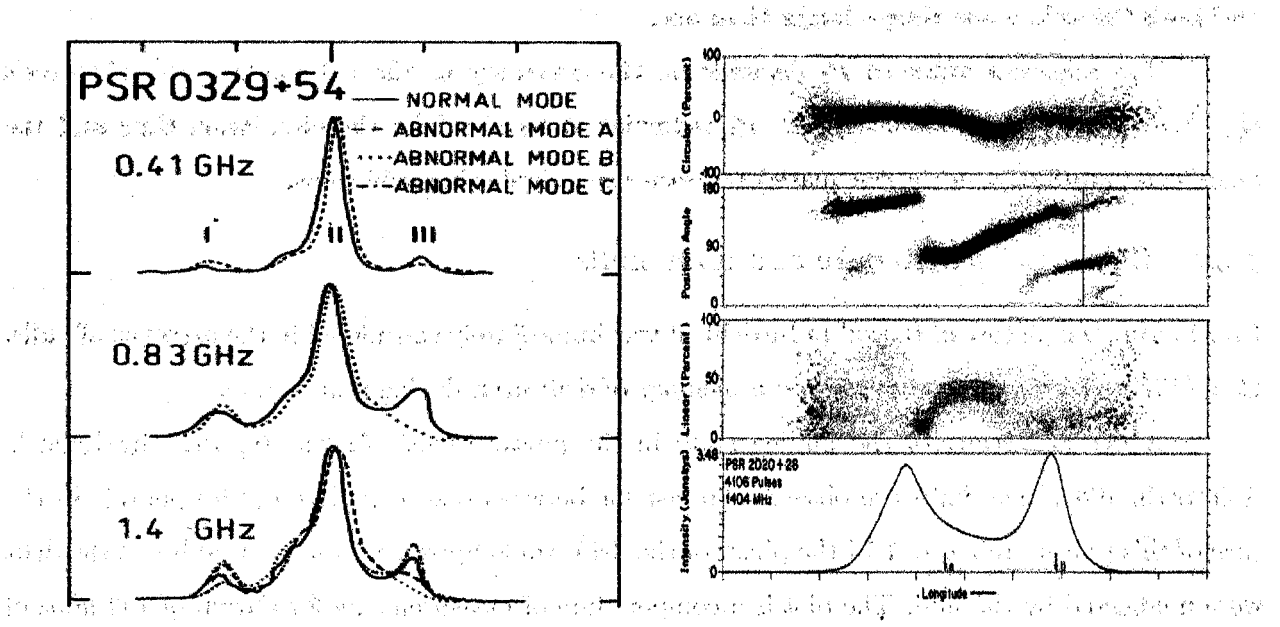

Figure 1.15: **Left:** Average-pulse,(total intensity) profiles of B0329+54 at three radio-frequencies in pulsar's normal and abnormal modes. Each pulse profile was averaged over $\gtrsim$ 2000 pulses at all three frequencies and was normalized to its peak value (from Rankin, 1986). Right: Orthogonal Polarization Modes in B2020+28 at 1404 MHz. Note that the degree of the linear polarization is the lowest at pulse longitudes where the two OPMs occur together (Stinebring et al., 1984).

ones. The emission restarts when the drift rate has partly recovered. For short nulls the drift does not completely halt.

1.2.5 Profile and polarization modes

Average profiles of pulsars are known for their long-term stability, and are related to structural properties of the emission cone. The modulations on the average properties axe associated with the plasma emission properties. Surprisingly, in some pulsars, the average profiles exhibit several, apparently discrete, stable forms. Such alterations of the average profiles are known as profile "mode changes" (figure 1.15). Pulsars may stay in the other modes for a few tens or hundreds of periods, after which they revert back to their 'normal' mode.

Mode changing is most easily identified in stars with triple and multiple profiles, but sometimes has been identified in S_d and D pulsars as well. It is typically characterized by a reorganization of the core and conal components of emission within the profile. The intensity of the core component is frequently enhanced in "abnormal" modes, and the symmetry of the conal components is affected. Mode changes induce slight shifts in the longitude positions of components (or the associated polarization signatures) and marked changes in the subpulse fluctuation patterns. Mode

changing is also known to affect the interpulse emission in B1822-09. All the observations suggest that mode changes signify physical changes of global extent in the polar regions.

We reviewed earlier the single-pulse fluctuations over and above the integrated pulse properties. As noted, even the polarization of an individual pulse fluctuates around the average, which can be easily seen as one plots the polarization angle as a function of longitude for individual pulses together. Such a plot, see figure 1.15, shows the presence of a component with polarization orthogonal to the average, In fact, the changing dominance of one mode over the other, as a function of pulse longitude, seems to account for observed 90° flips/discontinuities in an otherwise monotonic 'S'-curve and other discontinuities.

1.2.6 Conventional tools of study

We now consider various well-known techniques to study the phenomepa listed earlier in the chapter.

The average profile studies and the mode changing phenomena are studied' by folding the observed time series at an appropriate period of the pulsar in all the Stokes parameters. Figure 1.15 displays all such known information in a compact form.

Any fluctuations beyond the observed integrated profile are studied by looking at the fluctuations in individual pulses over the average profile. The region of longitudes containing the pulse region of interest is chosen, and a 2-D matrix of a Stokes parameter, in longitude and pulse number, is analyzed. Any phase or amplitude modulation is best studied by applying Fourier analysis to the Stokes Parameter, I (a 2-D matrix). First introduced by Backer (1973), this technique of the 'longitude-resolved fluctuation spectrum' allows one to study those modulations which sometimes may not be so apparent in individual pulses, or in the time domain.

A measure of the modulation power present at a particular longitude is also useful. The index of modulation underlines the degree,to which the different components of the average profile are affected by subpulse modulations.

Another way to study subpulse modulations is to study the auto-correlation of the profile and the cross-correlation of fluctuations in intensities between different longitude bins. One plots the correlation coefficientin a 2-D longitude against longitude plot (Kardashev et al., 1986). Modulations, which often appear less stationary and weak in the fluctuation spectral analysis, are likely to be more visible in such a plot.

These techniques are detailed in chapter 4 of this thesis.

1.3 Low-frequency considerations

Most of the observations pertaining the average and single-pulse properties outlined so far are usually carried out at meter and decimeter wavelengths. The decametric emission of pulsars is relatively less-studied. This is due to various difficulties in achieving high temporal resolution and sensitivity. Some of them arise due to the long path-length of the signal through the interstellar medium, and some due to conditions internal to the pulsar emission. These effects, and possible ways of dealing with them are outlined below.

1.3.1 Propagation effects

A variety of effects in the interstellar medium (ISM) cause distortion of the signals passing through it. Many of these effects are observable only in the case of pulsed signals. Hence, pulsars are considered very important probes for studying the properties of the ISM. However, the study of the intrinsic properties of radiation from pulsars becomes difficult in the presence of these propagation effects. Here, we briefly describe effects relevant to our present work, and refer the reader to Hankins & Rickett, 1975 for more details.

Dispersion

This effect occurs due to the presence of free electrons in the ISM. The group velocity of (V_g) of a group of waves traveling in a homogeneous isotropic neutral plasma is given by,

$$V_g = c\sqrt{1 - \left(\frac{\omega_p}{\omega}\right)^2} \tag{1.17}$$

where, ω_p is the plasma frequency, w the wave frequency, and c is the speed of light. The plasma frequency is given by,

$$\omega_p = \sqrt{\frac{4\pi n_e e^2}{m_e}} \tag{1.18}$$

where, n_e is the electron density of the interstellar plasma, e and m_e are charge and mass of an electron respectively. Thus, in the presence of the plasma in the ISM, the group velocity of the radio waves is slightly less than the speed of light, and is a function of the wave frequency and electron density in the medium.

In the observational bandwidth, the pulse arrival as a function of frequency is variable, where the pulse at the higher end would appear earlier (see figure 1.16). The arrival time delay between two frequencies is given by,

$$t_2 - t_1 \simeq \frac{e^2}{2\pi m_e c}\left(\frac{1}{f_1^2} - \frac{1}{f_2^2}\right)\int_0^d n_e\, dl \tag{1.19}$$

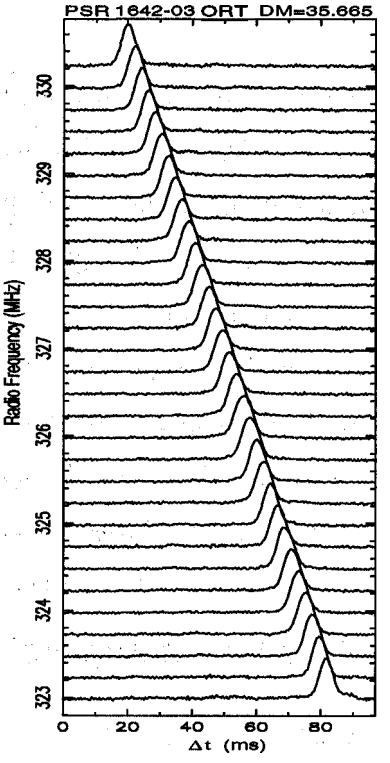

Figure 1.16: Pulse profiles of B1642-03 in 32 channels over an 8-MHz band without any dispersion correction. The dispersion delay in pulse arrival time between the channels is clearly visible. Over the 8-MHz band displayed, the pulse suffers a delay $\gtrsim$ 60ms (from Bhattacharya, 1997).

where, $\omega_p \ll 2\pi f_1, 2\pi f_2$, d is the distance to the pulsar, and $f_1 < f_2$. The above equation can be rewritten in the following form,

$$t_2 - t_1 \simeq \frac{DM}{2.41 \times 10^{-16}} \left(\frac{1}{f_1^2} - \frac{1}{f_2^2} \right) \tag{1.20}$$

where, DM (= $\int_0^d n_e \, \mathrm{dl}$) is called the dispersion measure of the pulsar. DM represents the column density of electrons along the entire path length to the pulsar, and is measured in the units of $parsec/cm^3$ or pc/cm^3, whereas the distance d is measured in parsec, and time in seconds.

If, further, we assume Af $= f_2 - f_1 \ll f_1, f_2$, then the equation above can be further simplified to,

$$\Delta t = \frac{DM \, \Delta f}{1.205 \times 10^{-4} \, f_0^3} \tag{1.21}$$

where, At is in seconds, and $\mathrm{A}f = f_2 - f_1$ and $f_0 = \sqrt{f_1 f_2} \simeq \left(\frac{f_1 + f_2}{2} \right)$ are in units of MHz.

Thus, if the pulsar signals were observed with a receiver channel bandwidth Af around a central frequency of f_0, then the pulses will be smeared by an amount At.

Dispersion removal scheme

If one were to combine the entire band as a single channel for pulsar observations, it would result in broadening the pulse due to differential dispersion delays across the band and, consequently, in loss of signal-to-noise ratio. One simple way of alleviating this problem is to split the full observing band into a number of narrow channels (as shown in figure 1.16), and record the time series in each channel separately in parallel. Later, suitable delays can be applied to the time series in each channel compensating the dispersion delay suffered in propagation. The signals from all the channels can be added in the end to yield a dispersion-corrected time sequence of intensity. This technique is known as incoherent dedispersion, since the delay correction is applied to the time series after detection. Figure 1.17 shows an example of reduction in the pulse smearing and improvement in the signal-to-noise ratio obtained employing this technique.

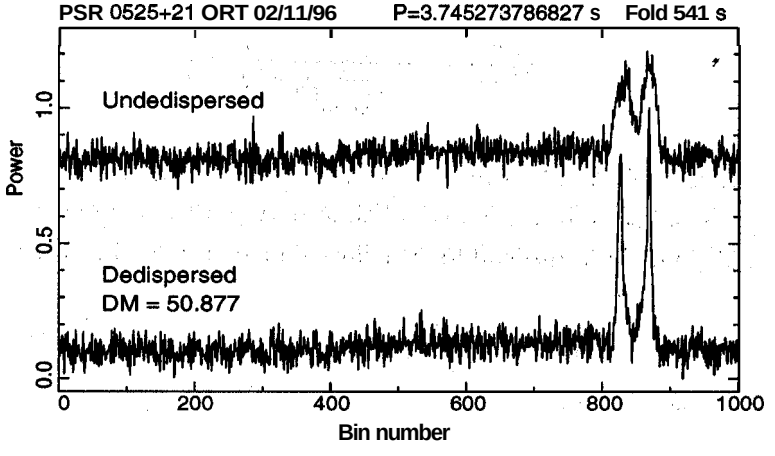

Figure 1.17: An example of incoherent dedispersion. PSR0525+21 was observed with 256 channels over an 8 **MHz** band centered on 327 **MHz.** The upper track shows the profile produced if no dispersion correction was applied between the channels, and the bottom panel shows the profile after an appropriate delay correction for the known DM (from Bhattacharya, 1997).

It is clear, however, that in the process of incoherent dedispersion the delay within each of the channels remains to be corrected. Therefore if the frequency channels are not narrow enough, the dispersion smearing may still dominate the pulse width, particularly for high values of **DM** and at low frequency. One can not have arbitrarily narrow frequency channels, one then comes up against another limit: a frequency channel of width $\Delta\nu$ will provide independent samples only at time intervals of $1/\Delta\nu$, *so* it is not possible to achieve a time resolution better than that. For a given frequency and DM, therefore, this suggests an optimum choice of channel width, below which the sampling limit prevails and above which the dispersion smearing dominates (Deshpande, 1989).

We consider it mare quantitatively in section 2.3.3.

Scattering & scintillations

The interstellar scattering is caused by the density irregularities in the electron density of the ISM (Scheuer, 1968). For a medium having electron density fluctuations Δn_e, with a characteristic scale size a, both of which may be functions of distance d along the line-of-sight, a plane wave front from a distant source is scattered through a range of angles θ_s, having an rms value θ_{rms} given by

$$\theta_{rms} \approx r_0 \frac{\lambda^2}{2\pi} (\Delta n_e) \sqrt{d/a} \tag{1.22}$$

where r_0 (= 2.8 x 10^{-13} cm) is the classical radius of the electron.

The apparent angular semi-diameter, θ_0, of the source is equal to $\theta_{rms}/2$.

For a scattering medium situated at mid-way between the source and the observer, the scattered radiation at a small angle (θ_s) is delayed with respect to the direct radiation by an amount

$$\text{t x } \frac{\theta_s^2 d}{2c} \tag{1.23}$$

Thus, in addition to the angular broadening, the scattering process causes time smearing of impulsive signals. For a Gaussian distribution of irregularity sizes and hence a Gaussian distribution of scattering angles, the pulse shape is effectively convoluted with a truncated exponential

$$S(t) = e^{-t/\tau_s} \tag{1.24}$$

where τ_s is the characteristic width of the impulse response representing scattering in the ISM, and $\tau_s = \theta_0^2 d/c$.

This time smearing has a strong dependence on the frequency of radiation and the distance between the source and the observer ($\propto d^2/\nu^{4.4}$).

Scintillations are caused by interference between the direct and scattered rays, which remain constructive only aver a limited bandwidth. Sutton (1971) has shown, that if Av is defined to be the frequency separation at which the correlation coefficient of observed intensity fluctuations drops to *0.5,* then

$$\Delta\nu = \frac{1}{2\pi\tau_s} \tag{1.25}$$

The intensity fluctuations as a function of time result from the passage of the telescope through the diffraction pattern formed by the screen of irregularities.

Faraday rotation

In the presence of even the weak magnetic fields in interstellar space, an effect called Faraday rotation becomes important. In this effect, the plane of polarization of a linearly polarized wave rotates along the propagation path. The angle of rotation after a traverse of a path d is

$$\text{All}, = \frac{2^{\pi e^3}}{(m\,c\,\omega)^2} \int_0^d n_e\, B_0\, cos(\theta)\, dl \tag{1.26}$$

where B_0 is the magnetic flux density, and 8 is the angle between the line-of-sight and the direction of the interstellar magnetic field.

The rotation measure of a background source is then defined by

$$\Delta\psi \;=\; RM\,\lambda^2 \tag{1.27}$$

so that

$$RM \;=\; \frac{e^3}{2\,\pi\, m^2 c^4} \int_0^d n_e\, B_0\, cos(\theta)\, dl \tag{1.28}$$

and, by convention, it is positive for fields directed toward the observer, and negative for the fields directed away.

The mean line-of-sight component of the magnetic field is given by

$$\langle B\, cos(\theta)\rangle \;=\; \frac{\int_0^d n_e\, B_0\, cos(\theta)\, dl}{\int_0^d n_e\, dl} \tag{1.29}$$

$$\;=\; 1.232\,(RM/DM) \tag{1.30}$$

where, B_0 is expressed in μ-gauss, RM in rad/m^2, and DM in pc/cm^3.

It should be noted, that for a given RM, the angle of rotation is a function of the observation wavelength. Therefore, if we observe over a bandwidth of Af around the central frequency f_0, such that $\Delta f \ll f_0$, the angles of rotation for the extreme frequencies within the band Af differ by an amount $\delta\psi$, given by

$$\delta\psi \;\simeq\; \frac{2\,RM\,c^2\,\Delta f}{f_0^3} \tag{1.31}$$

Hence, for studying the polarization characteristics, the receiver-channel bandwidths should be narrow enough, so that the intrinsic characteristics are not smeared much. However, due to the effects of the Faraday rotation, it becomes possible to effectively rotate the relative polarization of a receiving antenna by changing the observing frequency by appropriate amounts (Suleymanova, Volodin & Malofeev, **1983;** Smirnova & Boriakoff, **1997;** Ramkumar & Deshpande, **1998).**

1.3.2 Intrinsic effects

The propagation effects, discussed above, make high sensitivity and high time-resolution observations at low frequencies almost impossible for most of the distant pulsars. Apart from these effects, some intrinsic properties of pulsar emission pose additional difficulties.

Galactic background and turn-over in pulsar spectra

The galactic non-thermal background increases sharply at decameter wavelengths. The average sky temperature at 34.5 MHz is 10,000 K, (Dwarakanath & Uday Shankar, 1990), and it dominates over the receiver temperature. Pulsar spectra are well-approximated by a steep power law at meter wavelengths, with typical indices between -1 and -3 ($S_\nu \propto \nu^a$). The flux density spectra below $\sim$ 150 MHz, however, show a flattening or even a turn-over (Malofeev et *al.*, 1994). A typical example is shown in figure 1.18. Only in some exceptional cases, such as B0943+10 and the Crab, pulsar spectra show no deviation from a power law down to 35 MHz.

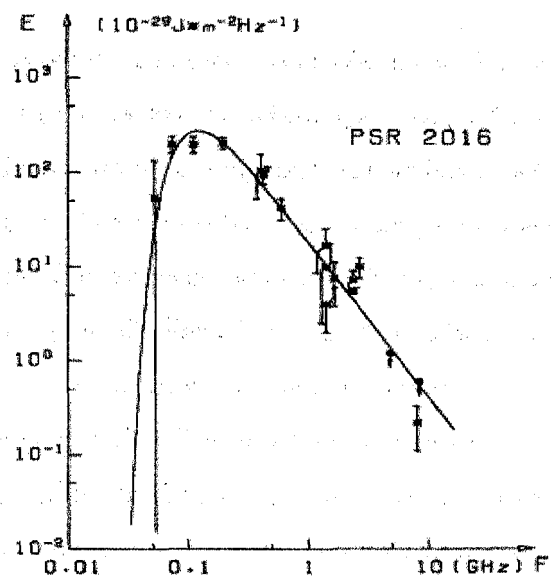

Figure 1.18: A spectrum of B2016+28 (Sieber, 1973). Typically, pulsars show a turnover in their spectra around 100 MHz.

Profile evolution

The average-pulse width of a pulsar is known to increase with wavelength (section 1.1.3), with a power law behavior, *i.e.* it goes as $\sim \nu^{-0.25}$. Hence, the peak signal-to-noise of the pulse reduces.

1.3.3 Interference

All observations at low radio frequencies are usually affected by interference. An interference localized in time or/and spectral domain can be easily identified and excised using standard techniques, either automatically or manually.

Our observations seem to be affected mainly by strong communication or radio broadcasting signals in our band. Such an interference was prevalent in the day-time, predominantly in late mornings and early evenings (about 9-11 am and 8-10 pm), when the ionosphere is relatively turbulent. Sun and low level thunderstorms may cause broadband interference in our data. Such an interference is usually spread over longer time and nonlocalised in frequency, making it harder to identify and excise. Our data analysis included interference excision as a routine step, and is described in section 2.3.3.

1.4 Detection & sensitivity considerations

Nyquist sampled signal voltages from the sky have zero mean and a certain *rms* (root mean square). When such a signal is detected using a square-law detector, the resultant time series is positive definite. It has a mean value equal to the total power in the band, and before integration, its *rms* is close to this mean. If such a signal is averaged over N independent samples, the mean of the resultant output remains the same, but the *rms* is reduced by a factor $\sqrt{N}$.

For a signal with a bandwidth of $\Delta\nu$, and available N_p polarizations (1 or 2), the total number of data samples aver an integration time of τ is $N_p \Delta\nu\tau$.

In a receiver, the 'noise' is contributed due to local electronics, termed as *receiver noise.* While observing, the sources in the the telescope beam, as well as diffuse background, give rise to it sky noise. The noise power in the receiver is usually measured in terms of its equivalent temperature T, defined by the noise power picked up by the dipole when immersed in a black-body bath of temperature T. The contribution of the receiver and sky noise are represented by $T_{rec}+T_{sky}$. The presence of the source in the beam is reflected in the enhancement of this noise temperature by T_A, which is given by

$$T_A = \frac{A_e S}{2 k_B} \tag{1.32}$$

where, S is the flux per unit frequency interval from the source, A, is the effective collecting area of the telescope and k_B is the Boltzmann constant.

We can, therefore, express signal-to-noise of the source in the following way. The off-source mean is $T_{rec}+T_{sky}$, and hence the off-source rms after integration is $(T_{rec}+T_{sky})/\sqrt{N_p \Delta\nu \tau}$. Since

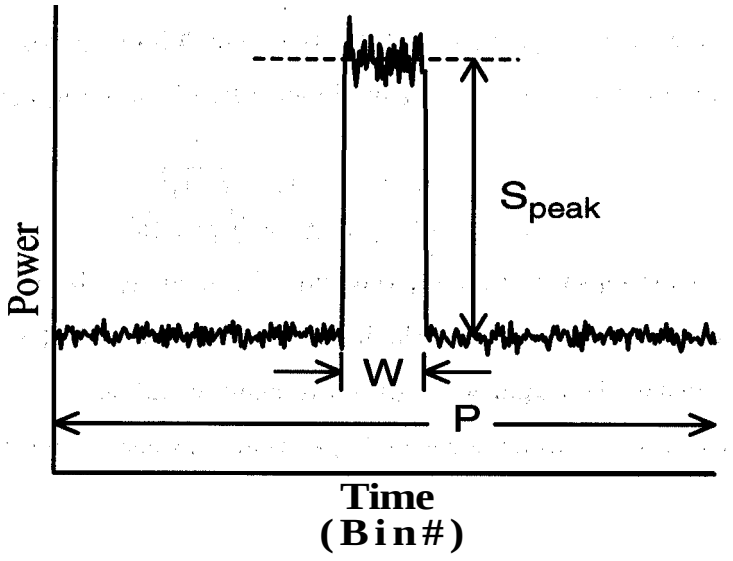

Figure 1.19: An idealized folded pulse profile. P is the pulse period, W is the pulse width and S_{peak} is the peak flux of the pulsar.

the excess temperature on-source is T_A, the signal-to-noise is

$$\mathrm{SNR} = \frac{}{T_{rec} + T_{sky}} \sqrt{N_p \, \Delta\nu \, \tau} \tag{1.33}$$

For a minimum SNR of β, the minimum detectable flux is given by,

$$S_{min} = \frac{\beta}{G} \frac{T_{rec} + T_{sky}}{\sqrt{N_p \, \Delta\nu \, \tau}} \tag{1.34}$$

where G (= $A_e/2k_B$) is the gain of the telescope.

In the case of a pulsar, the time series can be folded at the known period of the pulsar to enhance the signal-to-noise of detection. For such a folded pulse profile with a total of N_b bins across the entire period, the effective integration is τ/N_b. The peak of a folded profile (see figure 1.19) corresponds to a flux S_{peak}, which lasts for duration of W (pulse width) in every period. The minimum detectable flux for the pulse peak is,

$$S_{peak,min} = \frac{\beta}{G} \frac{T_{rec} + T_{sky}}{\sqrt{N_p \, \Delta\nu \, \tau}} \sqrt{N_b} \tag{1.35}$$

However, it is customary to quote the detection limit in terms of the average flux of the pulsar $S_avg = (W/P) \times S_{peak}$:

$$S_{avg,min} = \frac{\beta}{G} \frac{T_{rec} + T_{sky}}{\sqrt{N_p \, \Delta\nu \, \tau}} \sqrt{N_b} \frac{W}{P} \tag{1.36}$$

The best signal-to-noise is obtained if all the flux is collected into a single bin, *i.e.* $N_b = (P/W)$ for W $\ll$ P. For W $\geq P/2$, $N_b = P/(P - \mathrm{W})$. The following expression, widely used in the literature (Vivekanand, Narayan, & Radhakrishnan, 1982) is an interpolation between the two limits,

$$S_{avg,min} = \frac{\beta}{\mathrm{G}} \frac{T_{rec} + T_{sky}}{\sqrt{N_p \Delta\nu \tau}} \sqrt{\frac{W}{P - W}} \qquad (1.37)$$

In the equation for sensitivity above, the width W includes all broadening effects due to propagation in the interstellar medium and 'the instrumental response. The sharper the pulse, the better is the detectability of the pulsar for a given average-flux value.

If the pulse width of a pulsar becomes larger than the period due to broadening effects, it ceases to be a pulsar. Hence, distant, short period pulsars cannot be detected and studied at low frequencies like 34.5 MHz. From available measurements, we estimate that the farthest pulsar observable at decameter wavelengths is at a distance of $\lesssim$ 2 kpc.